



## Structure and photocatalytic performance of magnetically separable titania photocatalysts for the degradation of propachlor

V. Belessi <sup>a,b</sup>, D. Lambropoulou <sup>c</sup>, I. Konstantinou <sup>d</sup>, R. Zboril <sup>e</sup>, J. Tucek <sup>e</sup>, D. Jancik <sup>e</sup>, T. Albanis <sup>c</sup>, D. Petridis <sup>a,\*</sup>

<sup>a</sup> Institute of Materials Science, NCSR “Demokritos”, 15310 Aghia Paraskevi Attikis, Athens, Greece

<sup>b</sup> Department of Food Technology, Technological Educational Institution of Athens, Agiou Spyridonos Street, 12210 Egaleo, Athens, Greece

<sup>c</sup> Department of Chemistry, University of Ioannina, 45110 Ioannina, Greece

<sup>d</sup> Department of Environmental and Natural Resources Management, 30100 Agrinio, Greece

<sup>e</sup> Departments of Physical Chemistry and Experimental Physics and Nanomaterials Research Centre, Palacky University, Svobody 26, 77146 Olomouc, Czech Republic

### ARTICLE INFO

#### Article history:

Received 10 April 2008

Received in revised form 4 September 2008

Accepted 10 September 2008

Available online 26 September 2008

#### Keywords:

TiO<sub>2</sub>

γ-Fe<sub>2</sub>O<sub>3</sub>

Magnetically separated photocatalysts

Organic pollutants

### ABSTRACT

A magnetic photocatalyst was prepared by modification of TiO<sub>2</sub> nanoparticles (Degussa P25) with nanocrystalline γ-Fe<sub>2</sub>O<sub>3</sub> nanoparticles through a protective lining made up of two oppositely charged polyelectrolytes. As-prepared magnetically separable photocatalysts differing in γ-Fe<sub>2</sub>O<sub>3</sub> loading (3, 8, 13, 20 and 30 wt.%) were characterized by XRD, TEM, thermal analysis, Mössbauer and magnetic measurements. The photocatalytic efficiency of the nanocomposite catalysts was evaluated using a chloroacetanilide herbicide (propachlor) in water as model compound. The primary degradation of propachlor followed pseudo-first-order kinetics according to the Langmuir–Hinshelwood model. Generally, all magnetic photocatalysts exhibit good catalytic activity towards organic pollutants, do not suffer from photodissolution and can be reused several times without any decrease in their photocatalytic activity.

© 2008 Published by Elsevier B.V.

### 1. Introduction

Semiconductor photocatalysts have attracted much attention because of their potential application in the removal of organic and inorganic species from aquatic environments [1,2]. Nowadays, TiO<sub>2</sub> is widely recognized as the most promising photocatalyst for environmental applications. A major disadvantage of semiconductor oxides is the need of an additional and expensive separation step involving the removal of the photocatalyst from the treated water. In order to overcome this problem magnetically separable photocatalysts have been developed enabling the easy recovery of the photocatalyst by an external magnetic field [3–13].

The magnetic photocatalytic systems that have been developed so far contain magnetite (Fe<sub>3</sub>O<sub>4</sub>) or maghemite (γ-Fe<sub>2</sub>O<sub>3</sub>) [3–10] or spinel-like ferrites (NiFe<sub>2</sub>O<sub>4</sub>, Zn<sub>0.35</sub>Ni<sub>0.65</sub>Fe<sub>2</sub>O<sub>4</sub>) [11–13] serving as magnetic cores.

It has been established that direct contact between titanium oxide and iron oxide, i.e. TiO<sub>2</sub>/Fe<sub>3</sub>O<sub>4</sub> or TiO<sub>2</sub>/γ-Fe<sub>2</sub>O<sub>3</sub>, is responsible for low photoactivities because Fe<sub>3</sub>O<sub>4</sub> or γ-Fe<sub>2</sub>O<sub>3</sub> act as recombination centres for electrons and positive holes, especially in the

case of magnetite [3]. For example, it has been shown that the absorption of strong light by γ-Fe<sub>2</sub>O<sub>3</sub> nanoparticles causes low photocatalytic activity when the amount of γ-Fe<sub>2</sub>O<sub>3</sub> exceeds that of TiO<sub>2</sub> in the composite [5]. On the other hand, the use of a SiO<sub>2</sub> layer between the Fe<sub>3</sub>O<sub>4</sub> or γ-Fe<sub>2</sub>O<sub>3</sub> core and the TiO<sub>2</sub> shell, i.e. TiO<sub>2</sub>/SiO<sub>2</sub>/magnetic oxide, has been found to promote the photocatalytic activity of the catalyst by preventing the injection of charges from TiO<sub>2</sub> particles to magnetic particles [7,8]. In other words, the SiO<sub>2</sub> layer inhibits the photodissolution of the catalyst. In order to be then potentially applicable, the insulator has to be chemically inert and electronically passive toward titanium oxide.

Regarding the TiO<sub>2</sub>/spinel-ferrite systems, the TiO<sub>2</sub>/SiO<sub>2</sub>/Zn<sub>0.35</sub>Ni<sub>0.65</sub>Fe<sub>2</sub>O<sub>4</sub> photocatalyst shows high activity in the photo-oxidation of oxalate [12]. Similarly, the TiO<sub>2</sub>/SiO<sub>2</sub>/NiFe<sub>2</sub>O<sub>4</sub> photocatalyst displays enhanced photoactivity for decomposition of methylene blue [11]. Furthermore, the magnetically separable nitrogen-doped photocatalyst TiO<sub>2-x</sub>N<sub>x</sub>/SiO<sub>2</sub>/NiFe<sub>2</sub>O<sub>4</sub> is a good photocatalyst for the degradation of methyl orange, under UV and visible light irradiation [13]. However, the activity of the composite system was considerably lower than that of the pristine TiO<sub>2-x</sub>N<sub>x</sub> because of the non-perfect coating of SiO<sub>2</sub> around the surface of NiFe<sub>2</sub>O<sub>4</sub>.

Undoubtedly, the two important factors that determine the photoactivity, as well as the stability and the magnetic properties

\* Corresponding author. Tel.: +30 2106503343; fax: +30 2106519430.

E-mail address: dpetrid@ims.demokritos.gr (D. Petridis).

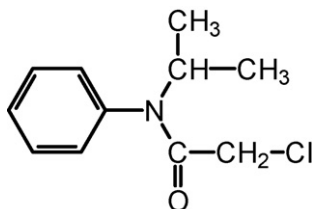


**Fig. 1.** The molecular structure of the herbicide propachlor.

of all photocatalysts, are the silica layer and the heat treatment during the preparation process. It has been demonstrated that the heat treatment step has important implications on the magnetite properties of the prepared photocatalysts due to chemical or physical changes of the magnetic core [3]. The use of calcined magnetic cores for the preparation for the preparation of  $\text{Fe}_3\text{O}_4$ - $\text{SiO}_2$ - $\text{TiO}_2$  [7] or  $\text{Zn}_{0.35}\text{Ni}_{0.65}\text{Fe}_2\text{O}_4$ - $\text{SiO}_2$ - $\text{TiO}_2$  [12] photocatalysts does not solve the problem, because the sol-gel synthesis of  $\text{TiO}_2$  requires a heating step for anatase growth.

This study is focused on overcoming the disadvantages from heating by exploiting the use of Degussa pristine  $\text{TiO}_2$  nanoparticles for the fabrication of stable magnetic photocatalysts. This novel method based on a protective lining made up of two oppositely charged polyelectrolytes avoids the heat treatment step and results in highly efficient and magnetically separable photocatalysts. The structural and magnetic nature of photocatalysts were investigated by several techniques and their photocatalytic efficiency was evaluated for degradation of propachlor, a chloroacetanilide herbicide (Fig. 1) that is commonly used.

## 2. Experimental

### 2.1. Materials

Ammonium peroxydisulfate  $(\text{NH}_4)_2\text{S}_2\text{O}_8$ , ammonium iron (II) sulphate hexahydrate  $\text{Fe}(\text{NH}_4)_2(\text{SO}_4)_2 \cdot 6\text{H}_2\text{O}$ , potassium hydroxide KOH, poly(diallyldimethylammonium)chloride 20 wt.% with typical  $M_w \sim 100,000$ – $200,000$  and poly(sodium 4-styrenesulfonate) average with typical  $M_w \sim 70,000$  were obtained from Aldrich and used as received. Commercial titania nanoparticles of P25 (ca. 80% anatase, 20% rutile, BET area ca.  $50 \text{ m}^2/\text{g}$ ) were supplied by Degussa (Germany). Propachlor analytical standard was purchased from Riedel-deHaen (Seelze, Germany).

### 2.2. Preparation of materials

#### 2.2.1. Preparation of negatively charged maghemite $[\gamma\text{-Fe}_2\text{O}_3/\text{PSS}^-\text{Na}^+]$

At first  $\gamma\text{-Fe}_2\text{O}_3$  was prepared according to the following procedure. To a solution of 2 g of  $\text{Fe}(\text{NH}_4)_2(\text{SO}_4)_2 \cdot 6\text{H}_2\text{O}$  in 50 mL of distilled water a solution of 1.14 g KOH in 30 mL of  $\text{H}_2\text{O}$  was added followed by 0.20 g of  $(\text{NH}_4)_2\text{S}_2\text{O}_8$  in 20 mL of  $\text{H}_2\text{O}$ . The black mixture was homogenized with magnetic stirring and kept at 60 °C for 1 h. The precipitated magnetic solid was cooled to room temperature, separated from the solution by centrifugation (1000 rpm/2 min), washed with deionized water (2× 50 mL), peptized in a 0.01 M hydrochloric acid solution under magnetic stirring for 1 h, re-centrifuged and finally dispersed in water (pH 4.5,  $Z = -10 \text{ mV}$ ). Negatively charged  $\gamma\text{-Fe}_2\text{O}_3$  nanoparticles were fabricated by wrapping the surface of the magnetic oxide with a 2 wt.% solution of poly(sodium 4-styrene sulfonate) polyanion ( $\text{PSS}^-\text{Na}^+$ ). The resulting product was left under stirring for 2 h (pH 5.7,  $Z = -45 \text{ mV}$ ,  $S \approx 2100 \text{ nm}$ ). Subsequently, the product was isolated by centrifugation, washed with deionized water (2×

50 mL), redispersed in 50 mL water, stirred overnight (pH 5,  $Z = -23 \text{ mV}$ ,  $S \approx 350 \text{ nm}$ ) and isolated by centrifugation. The product is labelled as  $[\gamma\text{-Fe}_2\text{O}_3/\text{PSS}^-\text{Na}^+]$ .

In a similar manner, a sample was prepared by reacting the  $[\gamma\text{-Fe}_2\text{O}_3/\text{PSS}^-\text{Na}^+]$  with the positively charged poly(diallyldimethylammonium)chloride ( $\text{PDD}^+\text{Cl}^-$ ) polyelectrolyte, i.e.  $[\gamma\text{-Fe}_2\text{O}_3/\text{PSS}^-\text{/PDD}^+]$ . This  $\gamma\text{-Fe}_2\text{O}_3$  derivative has a positive charge ( $Z = +40 \text{ mV}$ ).

#### 2.2.2. Preparation of positively charged $\text{TiO}_2$ particles

Because of the amphoteric nature of  $\text{TiO}_2$ , the surface charge of  $\text{TiO}_2$  nanoparticles can be controlled by adjusting the pH of the colloidal suspension below or above the isoelectric point of  $\text{TiO}_2$  (pH 6.3). Positively charged  $\text{TiO}_2$  was prepared using poly(diallyldimethylammonium) chloride solution as a positively charged binder to negatively charged  $\text{TiO}_2$  particles (pH 10). Specifically, a 0.5 wt.% suspension of  $\text{TiO}_2$ -P25 was prepared by stirring (pH 3.8,  $Z = +18 \text{ mV}$ ,  $S \approx 500 \text{ nm}$ ). The pH of the suspension was adjusted to 10 by a NaOH solution 20% w/v (pH 10,  $Z = -19 \text{ mV}$ ,  $S \approx 600 \text{ nm}$ ). Then a 5 wt.% solution of poly(diallyldimethylammonium) chloride was added and the resulting mixture was stirred for 2 h (pH 10,  $Z = +54 \text{ mV}$ ,  $S \approx 1100 \text{ nm}$ ). The resulting solid was isolated by centrifugation, washed with deionized water (2× 50 mL), dispersed in water and stirred overnight (pH 7.7,  $Z = +48 \text{ mV}$ ,  $S \approx 620 \text{ nm}$ ). The solid was isolated by centrifugation and air dried by spreading on a glass plate. It is labelled as  $[\text{TiO}_2/\text{PDD}^+\text{Cl}^-]$ .

#### 2.2.3. Preparation of $[\gamma\text{-Fe}_2\text{O}_3/\text{PSS}^-\text{/PDD}^+/\text{TiO}_2]$ photocatalyst particles

A colloidal dispersion containing appropriate amount of negatively charged maghemite particles in the form of  $[\gamma\text{-Fe}_2\text{O}_3/\text{PSS}^-\text{Na}^+]$  was added dropwise to a positively charged titanium oxide dispersion in the form of  $[\text{TiO}_2/\text{PDD}^+\text{Cl}^-]$  under continuous stirring and the mixture was left under stirring for 1 h (pH 6.3–6.4,  $Z = (+35)$ – $(+45) \text{ mV}$ ,  $S \approx 620$ – $700 \text{ nm}$ ). The product was isolated by centrifugation, washed with deionized water (2× 50 mL), redispersed in water and stirred overnight (pH 5.4,  $Z = (+26)$ – $(+35) \text{ mV}$ ,  $S \approx 350$ – $1000 \text{ nm}$ ). Five samples containing nominally 3, 8, 13, 20 and 30 wt.%  $\gamma\text{-Fe}_2\text{O}_3$  were prepared. The samples are denoted as Fe(3)Ti, Fe(8)Ti, Fe(13)Ti, Fe(20)Ti and Fe(30)Ti, meaning, for example that Fe(3)Ti is nominally  $[\gamma\text{-Fe}_2\text{O}_3(3\%)/\text{PSS}^-\text{/PDD}^+/\text{TiO}_2(97\%)$ .

### 2.3. Characterisation of photocatalysts

X-ray powder diffraction (XRD) patterns were recorded by a D-500 Siemens diffractometer using  $\text{Cu K}\alpha$  radiation ( $\lambda = 1.5418 \text{ \AA}$ ). Zeta-potential measurements were carried out on a Zeta Sizer instrument (Malvern Instruments) using the electrophoresis method. The measurements based on electrophoretic mobility of the nanoparticles in diluted aqueous suspensions were performed at least in triplicate with independent particle batches. Thermal analysis measurements were conducted under air flow with a temperature ramp of 10 °C/min on a PerkinElmer Thermogravimetric/Differential Analyser. Zero-field Mössbauer spectra were collected at 5 K in a constant acceleration mode with a 50-mCi  $^{57}\text{Co}(\text{Rh})$  source moving at room temperature, while the sample was placed in a variable temperature cryostat. Isomer shift values are reported with respect to  $\alpha\text{-Fe}$ . In-field Mössbauer measurements were performed at a temperature of 5 K in an external magnetic field of 5 T applied parallel to the gamma-ray direction (Oxford Instruments). A superconducting quantum interference device (SQUID, MPMS XL-7, Quantum Design) was used for magnetic measurements. The hysteresis loops were recorded at 2 and 300 K in external magnetic fields ranging from  $-7$  to  $+7 \text{ T}$ . The percentage of  $\text{TiO}_2$  and  $\gamma\text{-Fe}_2\text{O}_3$  in the samples was

calculated from energy dispersive spectra (EDS) measurements recorded on a Scanning Electron Microscope Jeol JSM 5600 operating at 20 kV.

The particle size and morphologies of  $\gamma\text{-Fe}_2\text{O}_3\text{-TiO}_2$  composites were evaluated from TEM micrographs using a JEM2010 microscope operating at 200 kV and characterized by a point-to-point resolution of 1.9 Å. Before measurements the samples were dispersed in ethanol and the suspensions were treated in ultrasound for 10 min. Following, a drop of very dilute suspension was placed on a carbon-coated grid and allowed to dry by evaporation at ambient temperature.

UV-vis absorption spectra of  $\text{TiO}_2$  nanocomposites were recorded in reflectance mode using a UV-vis spectrophotometer (Lambda 35, PerkinElmer Instruments) over the 200–800 nm range. Elemental chemical analysis (C, H, N, S) was performed in a PerkinElmer model 2400 Series II analyzer.

#### 2.4. Irradiation and analytical procedures

Irradiation of 70 mL aqueous propachlor solutions (5 mg/L) was performed in a batch Duran glass UV-reactor equipped with a water-circulating circuit. The concentration of photocatalyst slurries was set at 200 mg/L. All solutions were stirred for 30 min in the dark to allow equilibrium at neutral pH. Degradations were performed using a Suntest CPS+ apparatus from Heraeus (Hanau, Germany) equipped with a xenon arc lamp (1500 W) and special glass filters restricting the transmission of wavelengths below 290 nm. An average irradiation intensity of 750 W/m<sup>2</sup> was maintained throughout the experiments. The temperature was controlled (25 °C) by pressurized air-cooling circuit and monitored using thermocouples supplied by the manufacturer. Samples (1 mL) taken at different time intervals of irradiation in separate runs were centrifuged at 4500 rpm and the supernatant was analyzed by HPLC-UV, quantified by internal standard. Residual determination was performed using a Shimadzu HPLC (SPD-M10A-UV/diode array) equipped with a Discovery-C<sub>18</sub> column (Supelco) (5 µm, 25 cm × 4.6 mm i.d.) at the following conditions: mobile phase H<sub>2</sub>O/ACN (50/50 at 0 min, 30/70 at 15 min, 0/100 at 17 min, 50/50 at 19 min, total run time 20 min).

### 3. Results and discussion

#### 3.1. Characterization of $\gamma\text{-Fe}_2\text{O}_3\text{/PSS}^-\text{/PDD}^+\text{/TiO}_2$ nanocomposites

The composite  $\text{TiO}_2$  photocatalyst is made up of a magnetic particle ( $\gamma\text{-Fe}_2\text{O}_3$ ) lined with a thin membrane from two oppositely charged polyelectrolytes PSS<sup>-</sup>/PDD<sup>+</sup> to which the Degussa P25  $\text{TiO}_2$  nanoparticles are attached. The XRD pattern of the positively charged  $\text{TiO}_2$  particles  $[\text{TiO}_2\text{/PDD}]^+\text{Cl}^-$  (Fig. 2) gives the characteristic diffraction peaks of anatase and rutile because the pristine material ( $\text{TiO}_2$ -Degussa P25) contains both phases (80% anatase and 20% rutile). The strongest peak at  $2\theta = 25.2^\circ$  arises from the (1 0 1) anatase phase reflection and when applying the Debye-Scherrer formula to this reflection, the size of  $\text{TiO}_2$  crystallites was estimated between 20 and 24 nm. The XRD pattern of the negative charged maghemite  $[\gamma\text{-Fe}_2\text{O}_3\text{/PSS}]^-\text{Na}^+$  (Fig. 2) shows characteristics reflections at  $2\theta = 30.1$  (2 2 0), 35.5 (3 1 1), (37.2) (2 2 2), 43.1 (4 0 0), 53.4 (4 2 2), 57.0 (5 1 1) and 62.6 (4 4 0) indicating formation of a nanocrystalline spinel phase either of  $\text{Fe}_3\text{O}_4$  or  $\gamma\text{-Fe}_2\text{O}_3$  with an average size of 17 nm. Since these oxides are isostructural and, moreover, exist in nanoparticle state their XRD identification is difficult. The Mössbauer results that follow discern the two oxides and recognize conclusively the formation of maghemite. On the other side, the XRD spectrum of the composite

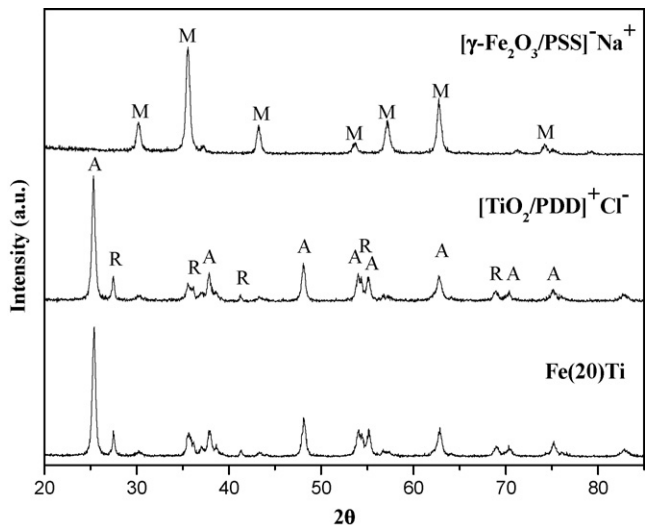


**Fig. 2.** XRD patterns of the negatively charged maghemite particles  $[\gamma\text{-Fe}_2\text{O}_3\text{/PSS}]^-\text{Na}^+$ , of the positively charged  $\text{TiO}_2$  particles  $[\text{TiO}_2\text{/PDD}]^+\text{Cl}^-$  and of the magnetic photocatalyst  $\text{Fe}(20)\text{Ti}$ .

$\text{Fe}(20)\text{Ti}$  shows clearly the reflections of  $\gamma\text{-Fe}_2\text{O}_3$ , anatase and rutile, as shown in Fig. 2.

The extent of the polyelectrolyte coatings in the representative  $\text{Fe}(20)\text{Ti}$  catalyst was examined by TG/DTA analysis. The DTA curve reveals a small endothermic peak at  $\approx 50^\circ\text{C}$  indicating the evaporation of volatile organic compounds and a large exothermic peak at the temperature range of  $120\text{--}520^\circ\text{C}$  due to the combustion of the thin organic polyelectrolyte membrane attached to the surface of the oxides (Fig. 3). The TG curve shows that the decomposition process in air was completed at  $\approx 520^\circ\text{C}$  with a mass loss of 3% in the temperature interval of  $120\text{--}520^\circ\text{C}$ . This is further confirmed by the elemental analysis of the  $\text{Fe}(20)\text{Ti}$  catalyst showing a percentage composition of C = 1.59%, H = 0.26%, N = 0.51% and S = 0.92%, which corresponds to a percentage composition of the organic polyelectrolyte membrane of 3.28%.

Representative TEM images of the  $\text{Fe}(20)\text{Ti}$  catalyst are presented in Fig. 4. The general TEM micrograph (see Fig. 4a) shows that the sample is composed of large clusters, the formation of which is evidently related to the electrostatic interactions between the positively charged  $\text{TiO}_2$  and negatively charged  $\gamma\text{-Fe}_2\text{O}_3$  nanoparticles and to magnetostatic interactions. The detailed zoom of a cluster (see Fig. 4b) indicates two types of

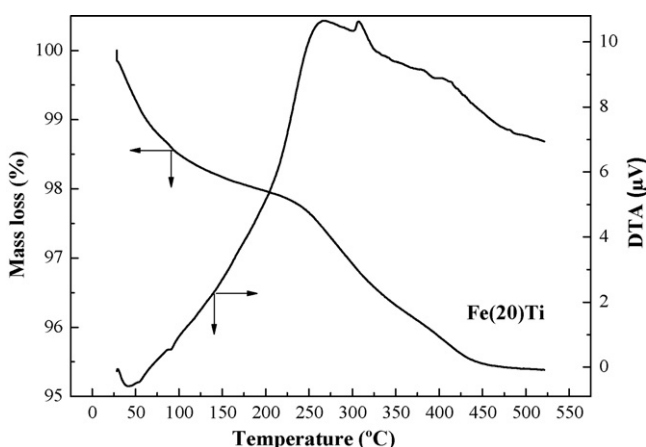


**Fig. 3.** TG-DTA curves of the  $\text{Fe}(20)\text{Ti}$  catalyst.

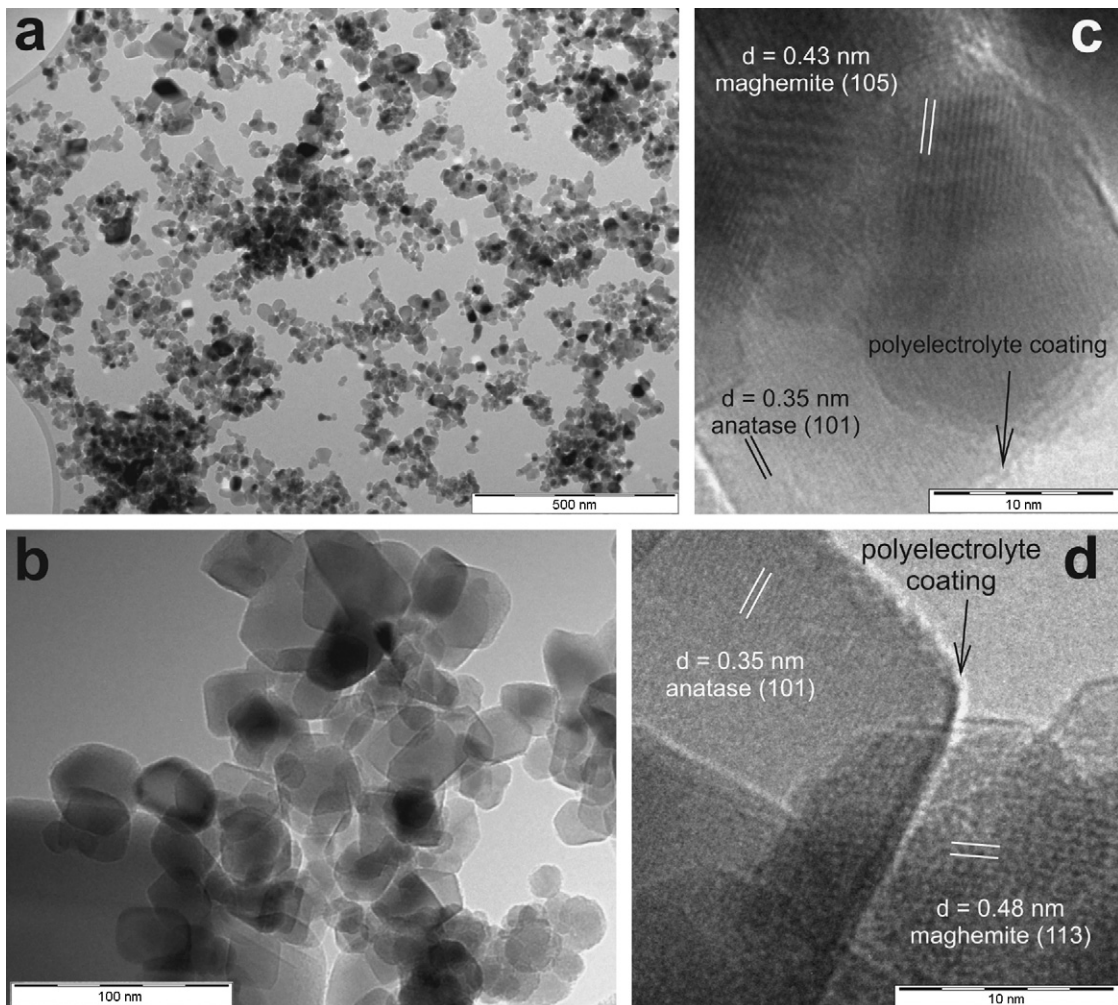


**Fig. 4.** TEM micrographs of the Fe(20)Ti catalyst. General view (a); detailed zoom of a cluster (b); high-resolution images showing the anatase crystal being in direct surface interaction with maghemite nanoparticle through the polyelectrolyte layers (c) and (d).

particles: globular crystallites of lower size and larger hexagonal particles that predominate. The globular particles can be clearly assigned to maghemite by measurement of interplanar distances in the high-resolution images, while the hexagons correspond to the anatase structure (see Fig. 4c and d). Also, from the same figures (i.e. Fig. 4c and d) we could see anatase crystal being in direct surface interaction with the maghemite nanoparticle through the narrow polyelectrolyte layer ( $\sim 1$  nm) that is clearly seen on the surface of both anatase and maghemite nanoparticles. It is worth to mention that TEM images do not reflect the interaction of the oxidic nanoparticles exactly due to the sample pre-treatment (sonication).

The zero-field and in-field Mössbauer spectra of the Fe(20)Ti sample, recorded at 5 K, are depicted in Fig. 5 and the hyperfine parameters derived from fitting of the experimental data are listed in Table 1. Without applied field, the deconvolution of the spectrum profile results in two distinct sextets (Fig. 5a). Since no doublet component, originating from superparamagnetic relaxation, appears in the spectrum, one can conclude that within the time window of the experimental technique (i.e.  $10^{-8}$  s in the case of Mössbauer spectroscopy), all the  $\gamma\text{-Fe}_2\text{O}_3$  particles bounded to  $\text{TiO}_2$  particles are blocked at 5 K. The detailed analysis of the hyperfine parameters of the individual sextets indicates the presence of two non-equivalent iron positions (i.e. tetrahedral

and octahedral) in the structure of iron oxide phase. The isomer shift of the A-sextet with a value of 0.35 mm/s at 5 K is typical of  $\text{Fe}^{3+}$  ions in a high spin state (i.e.  $S = 5/2$ ) occupying tetrahedral positions in maghemite structure, while the isomer shift value of 0.49 mm/s at 5 K, derived for the B-sextet, agrees well with that reported for the octahedral maghemite sites filled with  $\text{Fe}^{3+}$  ions with  $S = 5/2$ . This is further supported by the quadrupole shift values tending to zero (i.e. highly symmetrical surroundings of the Fe nuclei) and the very similar hyperfine field values of both sextets at low temperatures. Since no traces of divalent iron were detected in the spectral profile, the presence of magnetite can be, within the experimental error of the measuring technique, fully excluded. In addition, the overall spectral profile is asymmetric, which is a characteristic feature of the low-temperature Mössbauer spectrum of maghemite. However, the synthesized iron oxide phase is not stoichiometric, as evidenced by the ratio of octahedral/tetrahedral sextet being approximately 7/3 which is far from the ideal value (5/3) expected for stoichiometric maghemite.

To further gain insight into the structural and magnetic characteristics of maghemite nanoparticles, the Mössbauer spectrum at 5 K in an external magnetic field of 5 T has been measured. As seen in Fig. 5b, the application of the external field leads to much better separation of the absorption lines in the spectrum which can be well fitted with two sextets that belong to particular non-

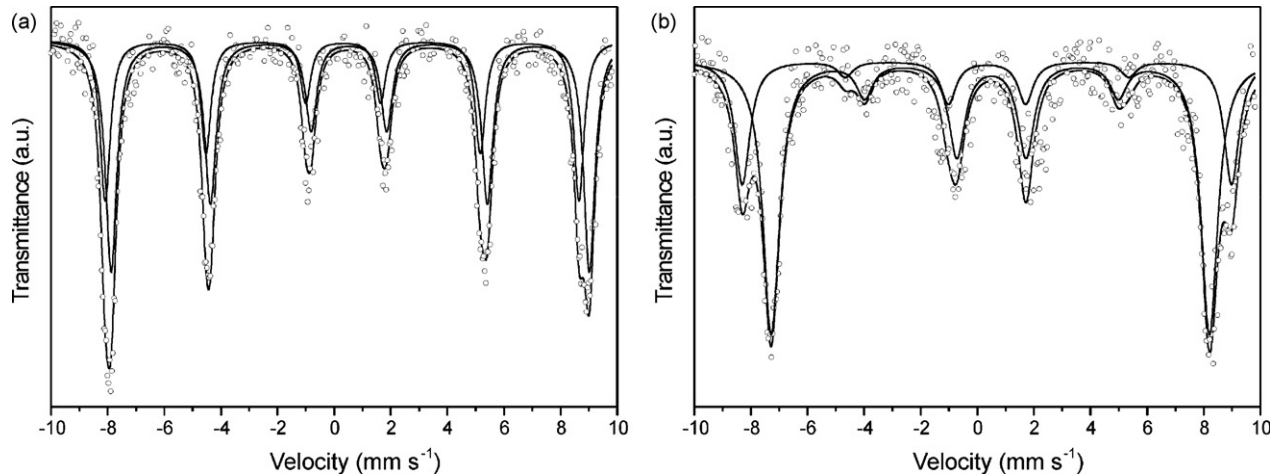


**Fig. 5.** Mössbauer spectra of the Fe(20)Ti sample, recorded at 5 K in a zero-field (a) and in a field of 5 T (b).

equivalent sites of the maghemite structure. In-field spectrum confirms the maghemite non-stoichiometry as the B/A ratio is 7/3 in accordance with the zero-field data. Since the external magnetic field was applied parallel to the direction of the  $\gamma$ -rays, it is expected that the 2nd and the 5th lines from  $\Delta m_l = 0$  transitions would be missing in the in-field Mössbauer spectrum, as the atomic spin moments from the tetrahedral and octahedral sites in an ideal ferrimagnetic maghemite align parallel and antiparallel to the applied magnetic field. However, this is not observed for the Fe(20)Ti sample for which the 2nd and the 5th lines have an appreciable intensity. In the assembly of the maghemite nanoparticles a portion of very fine particles with a high surface-to-volume ratio exhibits enhanced surface anisotropy and, therefore, a stronger applied magnetic field is required to align their surface magnetic moments compared to those perfectly coupled within the core of the particle. Thus, fine synthesized particles are said to show spin canting phenomenon, which is manifested by non-zero intensities of the 2nd and the 5th line in the in-field Mössbauer spectrum. In addition, there exists a probability for spin canting from bonding of  $\gamma\text{-Fe}_2\text{O}_3$  particles with  $\text{TiO}_2$  particles via coupling of surface atomic spins of  $\gamma\text{-Fe}_2\text{O}_3$  with those of  $\text{TiO}_2$ , giving thus an extra contribution to the local anisotropy. On the other hand, as the areas of the 2nd and the 5th lines are very narrow, the influence of spin canted maghemite sites on the magnetic properties of the synthesized sample is insignificant.

While Mössbauer spectroscopy gives information only on the magnetic behavior of iron-bearing phase, the magnetic measurements describe the overall magnetic response of a given  $\gamma\text{-Fe}_2\text{O}_3/\text{TiO}_2$  sample normalized to the mass of the studied powder. The hysteresis loop of the Fe(20)Ti sample recorded at 2 K (Fig. 6a) exhibits a hysteresis characterized by non-zero values of the coercivity and remanent magnetization, meaning that the magnetic moments within the individual particles behave at this temperature cooperatively which is manifested by an ordered state

of the investigated system. The hysteresis loop is shifted left and upward which is a typical feature frequently observed for nanosized materials. The average coercivity parameter ( $H_{C,\text{ave}} = (H_{C,+} + |H_{C,-}|)/2$ , where  $H_{C,+}$  is a positive coercivity and  $H_{C,-}$  is a negative coercivity, is found to be 390 Oe which is a result of contributions from both  $\gamma\text{-Fe}_2\text{O}_3$  and  $\text{TiO}_2$  particles. The saturation magnetization was found to be 11.4 emu/g of the composite material. This value is sufficiently high for effective magnetic separation of photocatalyst, however, much lower than that ( $\approx 60\text{--}80$  emu/g) reported for an assembly of only maghemite globular particles of comparable size distribution. The gradual rise of the magnetization at higher applied magnetic fields is attributed to the occurrence of spin canting which was confirmed by in-field Mössbauer spectroscopy. As temperature increases, the area of the hysteresis loop becomes smaller and at 298 K (Fig. 6b) the coercivity and saturation magnetization are approximately 20 Oe and 9.9 emu/g, respectively. The decrease in coercivity with raising temperature arises from the superparamagnetic behavior of the assembly of  $\gamma\text{-Fe}_2\text{O}_3$  particles. Thus, the key conclusion that results from the magnetization measurements is the sufficiently high magnetization of the Fe(20)Ti sample which saturates at relatively low applied fields at room temperature. This finding is then of a prime importance as it confirms the possibility of magnetic separation of the photocatalyst after its application.

UV-vis absorption spectra of the studied catalysts are depicted in Fig. 7. As expected, the  $[\text{TiO}_2/\text{PDD}]^+\text{Cl}^-$  derivative does not absorb beyond its fundamental sharp edge at 400 nm. In contrast the different  $\text{TiO}_2/\gamma\text{-Fe}_2\text{O}_3$  samples showed an absorption in the visible range due to the photosensitization of  $\gamma\text{-Fe}_2\text{O}_3$ . The absorption of  $\text{Fe}^{3+}$  in octahedral symmetry is known to appear at 430, 475 and 520 nm [14]. In the different  $\text{TiO}_2/\gamma\text{-Fe}_2\text{O}_3$  samples all bands from  $\text{Fe}^{3+}$  in octahedral symmetry are detected as long tails indicating that Fe component were linked to the external surface of the catalyst structure [15].

**Table 1**  
Mössbauer parameters of the Fe(20)Ti sample measured at 5 K in a zero field and in a field of 5 T.

T (K)	$B_{\text{ext}}$ (T)	Component	$\delta \pm 0.01$ (mm/s)	$\varepsilon_Q \pm 0.01$ (mm/s)	$B_{\text{hyp}} \pm 0.3$ (T)	$B_{\text{eff}} \pm 0.3$ (T)	$\text{RA} \pm 1$ (%)	Assignment
5	0	A-sextet	0.35	0.00	52.0	–	31	Tetrahedral $\text{Fe}^{3+}$
		B-sextet	0.49	-0.02	52.5	–	69	Octahedral $\text{Fe}^{3+}$
5	5	A-sextet	0.34	0.02	–	53.7	30	Tetrahedral $\text{Fe}^{3+}$
		B-sextet	0.50	-0.01	–	48.1	70	Octahedral $\text{Fe}^{3+}$

T is the temperature of measurement,  $B_{\text{ext}}$  the external magnetic field,  $\delta$  the isomer shift (with respect to metallic iron),  $\varepsilon_Q$  the quadrupole shift,  $B_{\text{hyp}}$  the hyperfine magnetic field,  $B_{\text{eff}}$  the effective magnetic field ( $B_{\text{eff}}$  is the vector sum of  $B_{\text{hyp}}$  and  $B_{\text{ext}}$ ) and RA the relative area of the individual sextets.

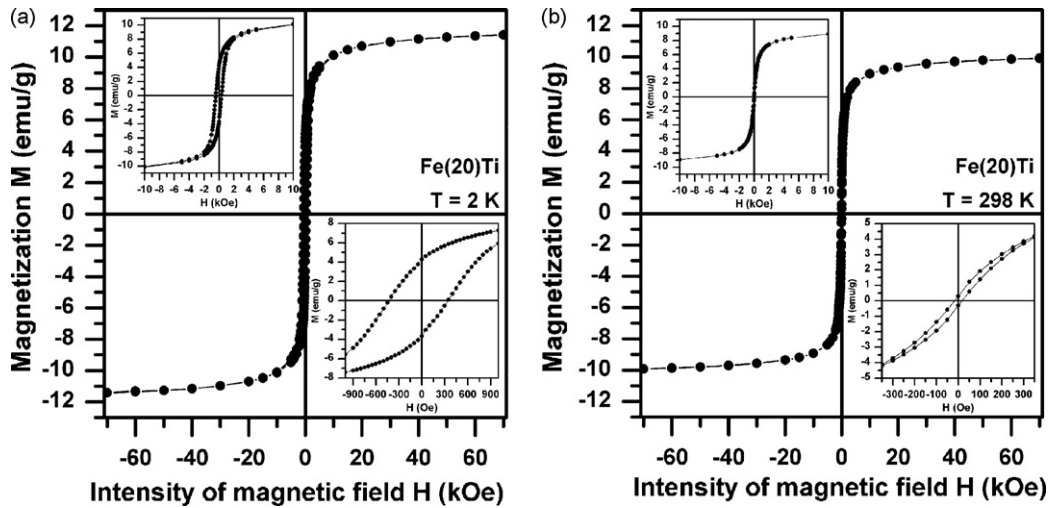


Fig. 6. Hysteresis loops of the Fe(20)Ti sample, measured at a temperature of (a) 2 K and (b) 298 K.

### 3.2. Photocatalytic performance

The photocatalytic performance of the  $[TiO_2/PDD]^+Cl^-$ ,  $[\gamma-Fe_2O_3/PSS^-Na^+]$ ,  $[\gamma-Fe_2O_3/PSS^-/PDD^+]$ , Fe(3)Ti, Fe(8)Ti, Fe(13)Ti, Fe(20)Ti and Fe(30)Ti composites for the photodegradation of propachlor is presented in Fig. 8 together with the performance of the commercial  $TiO_2$ -P25 for comparison. It has been shown that the photocatalytic oxidation of propachlor follows first-order kinetics according to the Langmuir–Hinshelwood model in agreement with the photocatalytic degradation of other pesticides [2,16]. The chemical composition of the photocatalysts, kinetic parameters and first-order model fitting are summarized in Table 2.

The photocatalytic activity of the samples, as summarized by the parameter  $k_{obs}$ , follows the order: P25 > Fe(20)Ti > Fe(13)Ti > Fe(30)Ti >  $[TiO_2/PDD]^+Cl^-$  > Fe(8)Ti > Fe(3)Ti >  $[\gamma-Fe_2O_3/PSS^-/PDD^+]$  >  $[\gamma-Fe_2O_3/PSS^-Na^+]$ . Comparing with pure  $TiO_2$ -P25 the photocatalytic efficiency of the prepared composite catalysts, especially Fe(20)Ti, is not much depressed. The  $[\gamma-Fe_2O_3/PSS^-Na^+]$  and  $[\gamma-Fe_2O_3/PSS^-/PDD^+]$  samples are not active in consistence with the fact that  $\gamma$ - $Fe_2O_3$  has little photocatalytic activity under UV irradiation. The  $[\gamma-Fe_2O_3/PSS^-/PDD^+]$  derivative showed higher activity than  $[\gamma-Fe_2O_3/PSS^-Na^+]$  probably due to

the higher adsorption of propachlor on the organophilic membrane covering the  $Fe_2O_3$  particles. For the  $[TiO_2/PDD]^+Cl^-$  catalyst, charged bilayers of  $PDD^+$  is believed to be formed on the  $TiO_2$  surface that are characterized by a hydrophobic interior that favors propachlor adsorption and a hydrophilic exterior that leads to disaggregation of semiconductor microparticles and to an increment of the surface area. However, it can be seen that the wrapping of  $TiO_2$ -P25 with the positive polyelectrolyte bilayer cause a significant reduction of its activity compared with  $TiO_2$ -P25. This means that the adsorption of the polyelectrolyte by the surfaces of  $TiO_2$ -P25 inhibits the photocatalytic degradation via blockage of reactive sites on the titanium oxide surface. In any case, the polyanion (e.g.  $[\gamma-Fe_2O_3/PSS^-Na^+]$ ), polycation (e.g.  $[TiO_2/PDD]^+Cl^-$ ) or polyanion/polycation (e.g.  $[\gamma-Fe_2O_3/PSS^-/PDD^+]$ ) membrane that wraps the  $\gamma$ - $Fe_2O_3$  or  $TiO_2$  nanoparticles do not promote their photocatalytic activity.

The photocatalytic activity of the composite samples follow the order  $Fe(20)Ti > Fe(13)Ti > Fe(30)Ti > Fe(8)Ti > Fe(3)Ti$ , where the photocatalytic activity for the Fe(13)Ti, Fe(20)Ti, and Fe(30)Ti catalysts is better than that of  $[TiO_2/PDD]^+Cl^-$ . The presence of polyelectrolytes on the surface of  $TiO_2$  reduces the effectiveness of this photocatalyst to a level similar to that of composite

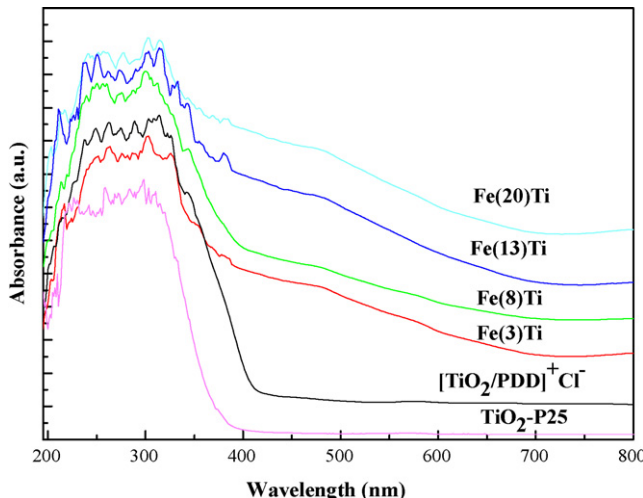


Fig. 7. UV-vis absorption spectra of the studied catalysts.

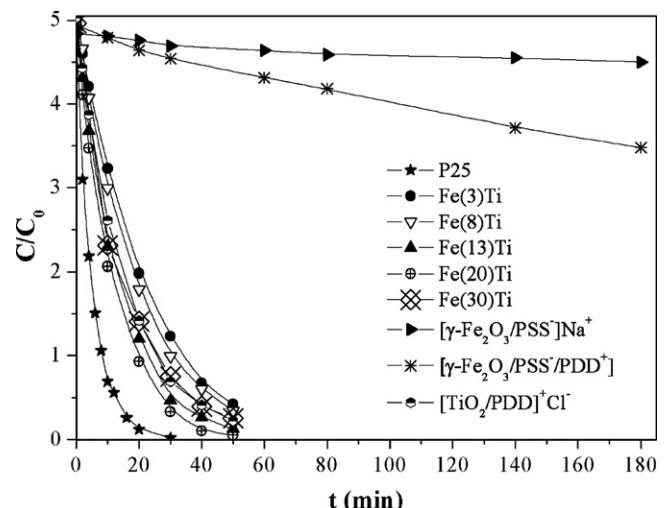


Fig. 8. Photocatalytic degradation kinetics of propachlor in  $[TiO_2/PDD]^+Cl^-$ ,  $[\gamma-Fe_2O_3/PSS^-Na^+]$ ,  $[\gamma-Fe_2O_3/PSS^-/PDD^+]$ ,  $\gamma$ - $Fe_2O_3$ - $TiO_2$  composites and  $TiO_2$ -P25 suspensions.

**Table 2**

Chemical composition of the different samples and kinetic parameters of propachlor degradation.

Photocatalyst (200 mg L <sup>-1</sup> )	$\gamma$ -Fe <sub>2</sub> O <sub>3</sub> (%)	TiO <sub>2</sub> (%)	$k_{\text{obs}}$ (min <sup>-1</sup> )	Linear correlation coefficient ( $R^2$ )	$t_{1/2}$ (min)
Fe(3)Ti	2.28	97.72	0.0495	0.9979	14.0
Fe(8)Ti	7.75	92.25	0.0538	0.9997	12.9
Fe(13)Ti	12.87	87.13	0.0749	0.9980	9.2
Fe(20)Ti	19.65	80.35	0.0938	0.9966	7.4
Fe(30)Ti	29.49	70.51	0.0711	0.9868	9.7
[ $\gamma$ -Fe <sub>2</sub> O <sub>3</sub> /PSS] <sup>-</sup> Na <sup>+</sup>			0.0004	0.9032	1732.9
[ $\gamma$ -Fe <sub>2</sub> O <sub>3</sub> /PSS <sup>-</sup> /PDD <sup>+</sup> ]			0.0019	0.9946	364.8
[TiO <sub>2</sub> /PDD] <sup>-</sup> Cl <sup>-</sup>			0.0628	0.9975	11.0
Degussa-P25			0.1838	0.9991	3.8

photocatalysts with fewer  $\gamma$ -Fe<sub>2</sub>O<sub>3</sub> percentages. This fact suggests that there is no recombination in  $\gamma$ -Fe<sub>2</sub>O<sub>3</sub> particles responsible for the loss effectiveness observed but another effect attributable to the presence of polyelectrolytes on the surface of TiO<sub>2</sub>.

According to the present literature, magnetic iron oxide-TiO<sub>2</sub> surfaces exhibit low activity compared with pure TiO<sub>2</sub>. This behavior has been attributed to the injection of charges from TiO<sub>2</sub> into  $\gamma$ -Fe<sub>2</sub>O<sub>3</sub> causing an “induced photodissolution” [3,5,8]. At this point, we note that the relative positions of the conduction and valence bands of the two semiconductors are crucial for the observed photoreactions. The conduction band of  $\gamma$ -Fe<sub>2</sub>O<sub>3</sub> ( $E_{\text{CB}} = 0.1$  V vs NHE at pH 7,  $E_g = 2.3$  eV) is lower than that of TiO<sub>2</sub> ( $E_{\text{CB}} = -0.5$  V vs NHE at pH 7,  $E_g = 3.2$  eV) and the valence band of  $\gamma$ -Fe<sub>2</sub>O<sub>3</sub> ( $E_{\text{VB}} = 2.3$  V vs NHE at pH 7) is higher than that of TiO<sub>2</sub> ( $E_{\text{VB}} = 2.7$  V vs NHE at pH 7) [8]. Thus, the photogenerated electrons on TiO<sub>2</sub> phase can be transferred into the lower lying conduction band of maghemite and the holes can be transferred to the upper lying valence of the iron oxide that can act, in this way, as a recombination centre.

It is also generally accepted that the insertion of an intermediate passive SiO<sub>2</sub> layer between titanium dioxide and iron oxide inhibits electrical contact and thus prevents photodissolution of the iron oxide phase [7,8,12,13]. In a similar manner, the thermodynamically feasible transfer of photogenerated electrons from the TiO<sub>2</sub> surface into the lower lying conduction band of the  $\gamma$ -Fe<sub>2</sub>O<sub>3</sub> does not take place in our TiO<sub>2</sub>/ $\gamma$ -Fe<sub>2</sub>O<sub>3</sub> samples. We believe that this is due to the thin PSS<sup>-</sup>/PDD<sup>+</sup> membrane separating the surfaces of TiO<sub>2</sub> and  $\gamma$ -Fe<sub>2</sub>O<sub>3</sub> nanoparticles, in accordance with TEM data. The membrane acts as an insulator [17] and prevents the injection of electron to the iron oxide surfaces. Accordingly, there are no competing reactions between the oxidation of propachlor and the Fe<sup>2+</sup>/Fe<sup>3+</sup> redox systems [7,18–21].

In order to support this aspect, a photodissolution test was carried out for the representative Fe(20)Ti catalyst. In the test 14 mg of the photocatalyst were suspended into 70 mL aqueous propachlor solution (5 mg/L) and the system was illuminated for 50 min. Then, a few drops from an alcoholic solution (10% wt) of 1,10-phenanthroline were added to a part of the supernatant. No red coloration was observed indicating the absence of any Fe<sup>2+</sup> ions in the solution. Similarly, the presence of Fe<sup>3+</sup> ions was examined by the addition of a few drops of KSCN solution to the other part of supernatant. No coloration was detected meaning the absence of trivalent iron ions. In addition, analysis with ICP spectrophotometry revealed the absence of Fe and Ti in the solution. The above tests prove the stability of the photocatalytic system and therefore no photodissolution phenomenon took place during the photocatalytic action.

The observed apparent kinetics could be due to the effect of the following parameters: (a) the adsorption of propachlor on the catalysts depending on the surface hydrophobicity, (b) the

effective reaction surface area depending on the particle dispersibility, and (c) the light absorption by the  $\gamma$ -Fe<sub>2</sub>O<sub>3</sub>. Preliminary adsorption experiments of propachlor into the various catalysts under the present experimental conditions showed that adsorption percentages were 14% for Fe(3)Ti, 15% for Fe(8)Ti, 19% for Fe(13)Ti, 20% for Fe(20)Ti and 17% for Fe(30)Ti. The addition of [ $\gamma$ -Fe<sub>2</sub>O<sub>3</sub>/PSS]<sup>-</sup> made the surface more hydrophobic, i.e. more susceptible for propachlor adsorption but at the same time the increased hydrophobicity resulted in worse dispersion in the aqueous suspension and strong light absorption by the  $\gamma$ -Fe<sub>2</sub>O<sub>3</sub> phase. The increased concentration of propachlor near the active sites of the semiconductor surface could justify the observed increase in the degradation rate for the catalysts up to 20% of  $\gamma$ -Fe<sub>2</sub>O<sub>3</sub> loading. Previous studies, in fact, supported the favourable influence of substrate adsorption onto surfactant modified TiO<sub>2</sub> on photocatalytic degradation [22–25]. Other investigators working with TiO<sub>2</sub> pillared clays have pointed out also that the order of performance in adsorption and successive photocatalytic degradation of organic pollutant was consistent with that of surface hydrophobicity [26]. This is also consistent with the Langmuir–Hinshelwood-type surface reaction mechanism that for dilute systems it is important to increase the surface concentration of substrates. However, increasing the percentage of  $\gamma$ -Fe<sub>2</sub>O<sub>3</sub> at 30% leads to lower photocatalytic activity probably as a result of worse dispersion of the catalyst in the water due to increased hydrophobicity and thus reduced surface area. Another factor that influences also the degradation rate could be the strong light absorption of the  $\gamma$ -Fe<sub>2</sub>O<sub>3</sub>.

In other case, there is a small possibility that the polyelectrolyte membrane could not separate completely the Fe<sub>2</sub>O<sub>3</sub>–TiO<sub>2</sub> surfaces and that TiO<sub>2</sub> and Fe<sub>2</sub>O<sub>3</sub> nanoparticles are in contact at some sites.  $\gamma$ -Fe<sub>2</sub>O<sub>3</sub> can act either as a scavenger or recombination center of electrons and holes depressing the activity of the photocatalyst or as a desirable electron acceptor. Electron binding aids the separation of electron–hole pairs in titania, enhances the concentration of the holes at the surface of titania and improves the activity of the photocatalyst [8]. The characteristic times of the injection of e<sup>-</sup> and h<sup>+</sup> from TiO<sub>2</sub> to  $\gamma$ -Fe<sub>2</sub>O<sub>3</sub> are shorter than 10 ns [27,28], while the time for reaction of e<sup>-</sup> with adsorbed O<sub>2</sub> is at the ms level and the reaction of h<sup>+</sup> with TiOH is about 10 ns [8,29]. Therefore, the injection of e<sup>-</sup> into the conduction band of  $\gamma$ -Fe<sub>2</sub>O<sub>3</sub> is much faster than the reaction with O<sub>2</sub> while the transfer of h<sup>+</sup> into the valence band of  $\gamma$ -Fe<sub>2</sub>O<sub>3</sub> and the reaction of h<sup>+</sup> have a ratio of 1–10. Although  $\gamma$ -Fe<sub>2</sub>O<sub>3</sub> wastes similar amount of holes and electrons, it plays a role in an effective separation of the e<sup>-</sup>/h<sup>+</sup> pairs in the titania which enhances the concentration of the holes at the surface of the titania [8]. The two opposite functions of the  $\gamma$ -Fe<sub>2</sub>O<sub>3</sub> surfaces have been demonstrated by Zhang and Lei [30] who studied the effect of Fe/Ti ratio on the photocatalytic efficiency of Fe<sub>2</sub>O<sub>3</sub>–TiO<sub>2</sub> coatings. They concluded that the optimal Fe/Ti ratio is

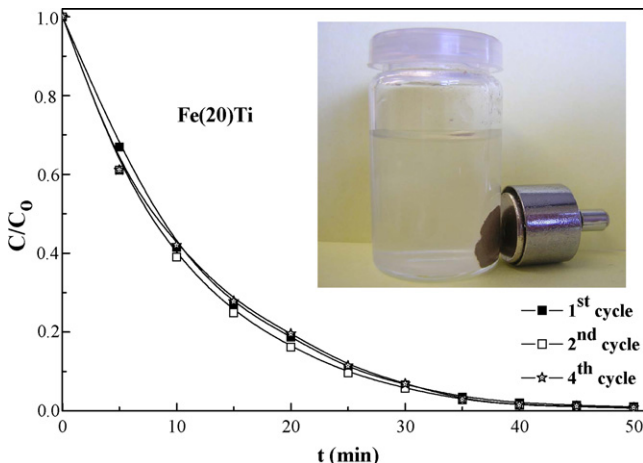


**Fig. 9.** Degradation of propachlor with recycled Fe(20)Ti catalyst after successive cycles. Inset: Illustration of the magnetic separation of the Fe(20)Ti photocatalyst from the liquid media.

0.24 and that above this ratio the  $\text{Fe}^{3+}$  centers become effective recombination centers and the activity steadily decreases.

The possibility of catalyst recovery and reuse in photocatalytic processes is of major importance, since it contributes significantly to lowering the operational cost of the wastewater treatment. In order to assess photocatalyst activity on repeated use, experiments were performed where the catalyst Fe(20)Ti was recovered and reused. The photocatalytic activity of the recycled catalyst has not noticeably changed after four successive cycles under UV-vis irradiation ( $\lambda > 290 \text{ nm}$ ) indicating that the magnetically separable photocatalyst is stable and effective for the decomposition of pesticides such as propachlor (Fig. 9). The effectiveness of magnetic separation process after the fourth cycle under UV-vis irradiation is illustrated in Fig. 9 inset, where a magnet was applied to attract the photocatalytic system. The results show that the photocatalyst can be separated rapidly compared to P25 after its use in suspension system. Furthermore, the Fe(20)Ti magnetic photocatalyst can be redispersed into aqueous solution after removing the magnet. No Fe or Ti particles were detected in the solution after the separation of the photocatalyst by a magnetic field after 1, 2 and 3 h under UV-vis illumination, as confirmed with inductively

coupled plasma-atomic emission spectroscopy ICP (ICP-AES) with the use of an Optima 3000 (PerkinElmer, USA) unit.

The overall stability of the Fe(20)Ti material is also documented by the measurement of hysteresis loops after different periods of UV-vis illumination and from TEM images (Fig. 10). The hysteresis parameters, derived from particular curves of magnetization vs. applied magnetic field, are practically the same (Fig. 10), meaning that the system retains its magnetic properties after UV-vis illumination. The stability of the Fe(20)Ti sample after 3 h of UV-vis illumination is further evidenced from TEM images where the presence of the polyelectrolyte layers, connecting maghemite nanoparticles with anatase is still clearly seen.

The recorded photocatalytic stability of the catalysts after repeated use under the present experimental conditions suggests the selective propachlor degradation but not the polyelectrolyte layers. Considering that OH radicals and positive holes are the main reactive species, propachlor is more easily oxidized than the polyelectrolytes because the positive charge on the head group of  $\text{PDD}^+$  reduces the probability for the addition of electrophilic strong oxidants such as OH radicals or positive holes. For aromatic compounds such as propachlor, electrophilic addition to the ring and secondly hydrogen and electron abstraction are more probable pathways. Previous photocatalytic degradation studies of propachlor with  $\text{TiO}_2$  [31] revealed that the principal degradation pathways involved the reaction of propachlor with OH radicals and holes. Thus, the oxidants preferentially attack propachlor rather than polyelectrolytes. In addition, when the Fe(20)Ti material was analyzed with TG after the 1 h photocatalytic cycle in the absence of propachlor, the weight loss was always less than 4% showing the stability of the materials under the present experimental parameters. Similarly, the preferential oxidation of organic compounds (2-naphthol) in the presence of surfactant bilayers (trimethylstearyl ammonium chloride— $\text{C}_{18}\text{TAC}$ ) formed on  $\text{TiO}_2$  was previously reported [22]. It is demonstrated that  $\text{C}_{18}\text{TAC}$  molecules on the  $\text{TiO}_2$  surface remained intact after 2 h irradiation in the presence of 2-naphthol, while they were oxidized in the absence of 2-naphthol.

In conclusion, it must be denoted that the observed degradation behavior reflects the complexity of the investigated system where various partition equilibria, particle dispersibility, light absorption and charge transfer simultaneously exert their influence on the photocatalytic treatment and where polyelectrolyte degradation

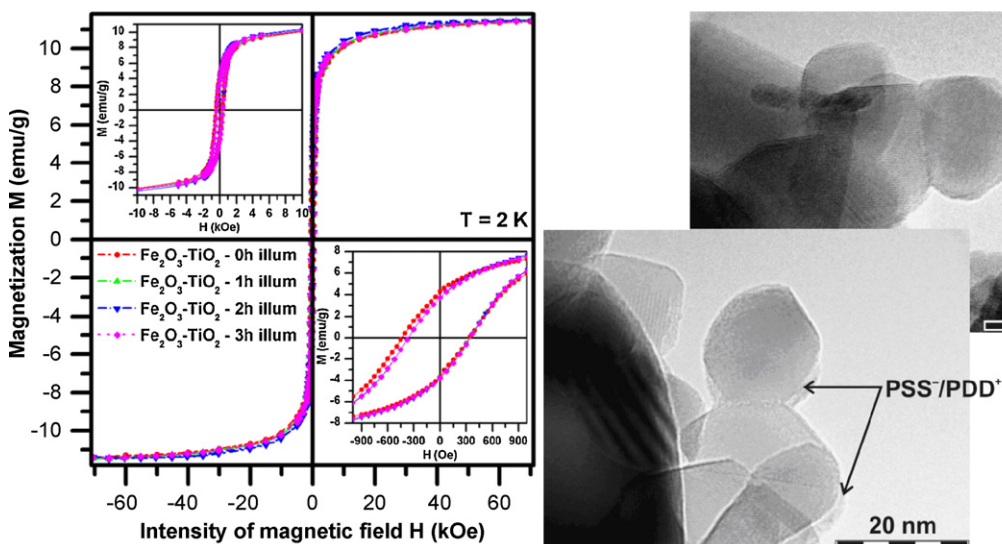


**Fig. 10.** Hysteresis loops, measured at a temperature of 2 K, for the Fe(20)Ti sample before and after UV-vis illumination for different periods of time (1 h, 2 h, 3 h) and TEM images of the Fe(20)Ti sample after 3 h of illumination demonstrating the stability of the nanocomposite system.

could play a role at longer irradiation times. Studies concerning these peculiar aspects of polyelectrolyte assisted photocatalysis together with the effect on the evolution of the degradation products could be examined in details in future studies.

#### 4. Conclusions

Using the polyelectrolyte templates, we prepared a novel kind of  $\gamma$ -Fe<sub>2</sub>O<sub>3</sub>/TiO<sub>2</sub> photocatalysts which can be easily separated by a magnetic field. The key components of these photocatalysts are the insulator polyelectrolytes that constitute the corrosion protective membrane between maghemite and titanium dioxide and they inhibit the negative influence of the  $\gamma$ -Fe<sub>2</sub>O<sub>3</sub> on the photocatalysis. The developed nanocomposites exhibit good catalytic activity towards organic pollutants such as chloroacetamide herbicides and they are only a little bit less efficient than the commercial photocatalyst Degussa P25, under the same experimental conditions. As-prepared magnetic photocatalysts are stable and do not suffer from photodissolution. Furthermore, they can be reused several times without any significant decrease of their photocatalytic efficiency which implies that they are promising candidates for the practical use in the wastewater treatment technologies.

#### Acknowledgements

This work has been supported by the Projects of the Ministry of Education of the Czech Republic (1M6198959201 and MSM6198959218) and by the project of ACSR (KAN115600801). We also thank Philippos Pomonis and Alexandros Katsoulidis at University of Ioannina for the Energy Dispersive Spectra (EDS) measurements as well as Dr. Christos Trapalis at NCSR “Demokritos” for the ICP analysis.

#### References

- [1] D.F. Ollis, H. Al-Ekabi (Eds.), Photocatalytic Purification and Treatment of Water and Air, Elsevier, Amsterdam, 1993.
- [2] I.K. Konstantinou, T.A. Albanis, *Appl. Catal. B: Environ.* 42 (2003) 319–335.
- [3] D. Beydoun, R. Amal, G.K.-C. Low, S. McEvoy, *J. Phys. Chem. B* 104 (2000) 4387–4396.
- [4] D. Beydoun, R. Amal, *Mater. Sci. Eng. B* 94 (2002) 71–81.
- [5] Y. Gao, B. Chen, H. Li, Y. Ma, *Mater. Chem. Phys.* 80 (2003) 348–355.
- [6] S. Watson, D. Beydoun, R. Amal, *J. Photochem. Photobiol. A: Chem.* 148 (2002) 303–313.
- [7] D. Beydoun, R. Amal, G. Low, S. McEvoy, *J. Mol. Catal. A: Chem.* 180 (2002) 193–200.
- [8] F. Chen, Y. Xie, J. Zhao, G. Lu, *Chemosphere* 44 (2001) 1159–1168.
- [9] S. Watson, J. Scott, D. Beydoun, R. Amal, *J. Nanoparticle Res.* 7 (2005) 691–705.
- [10] D. Beydoun, R. Amal, J. Scott, G. Low, S. McEvoy, *Chem. Eng. Technol.* 24 (2001) 745–748.
- [11] Y.S. Chung, S.B. Park, D.-W. Kang, *Mater. Chem. Phys.* 86 (2004) 375–381.
- [12] D.G. Shchukin, A.I. Kulak, D.V. Sviridov, *Photochem. Photobiol. Sci.* 1 (2002) 742–744.
- [13] S. Xu, W. Shangguan, J. Yuan, M. Chen, J. Shi, *Appl. Catal. B: Environ.* 71 (2007) 177–184.
- [14] S.H. Lee, M. Kang, S.M. Cho, G.Y. Han, B.W. Kim, K.J. Yoon, C.H. Chung, *J. Photochem. Photobiol. A* 146 (2001) 121–128.
- [15] M. Kang, S.-J. Choung, J.Y. Park, *Catal. Today* 87 (2003) 87–97.
- [16] V. Belessi, D. Lambropoulou, I. Konstantinou, A. Katsoulidis, P. Pomonis, D. Petridis, T. Albanis, *Appl. Catal. B: Environ.* 73 (2007) 292–299.
- [17] J.-A. He, R. Mosurkal, L.A. Samuelson, L. Li, J. Kumar, *Langmuir* 19 (2003) 2169–2174.
- [18] C. Pulgarin, J. Kiwi, *Langmuir* 11 (1995) 519–526.
- [19] A. Ansari, J. Peral, X. Domenech, R. Rodriguez-Clemente, A. Roig, E. Molins, *J. Photochem. Photobiol. A* 87 (1995) 121–125.
- [20] A. Ansari, J. Peral, X. Domenech, R. Rodriguez-Clemente, *Environ. Pollut.* 95 (3) (1997) 283–288.
- [21] E. Brillas, E. Mur, R. Sauleda, L. Sanchez, J. Peral, X. Domenech, J. Casado, *Appl. Catal. B: Environ.* 16 (1998) 31–42.
- [22] H. Tada, H. Matsui, F. Shiota, M. Nomura, S. Ito, M. Yoshihara, K. Esumi, *Chem. Commun.* 16 (2002) 1678–1679.
- [23] Q. Yuan, R. Ravikrishna, K.T. Valsaraj, *Sep. Purif. Technol.* 24 (2001) 309–318.
- [24] K. Inumaru, M. Murashima, T. Kasahara, S. Yamanaka, *Appl. Catal. B* 52 (2004) 275–280.
- [25] D. Fabbri, A. Bianco Prevot, E. Pramauro, *Appl. Catal. B* 62 (2006) 21–27.
- [26] C. Ooka, H. Yoshida, K. Suzuki, T. Hattori, *Micropor. Mesopor. Mater.* 67 (2004) 143–150.
- [27] A.M. Chaparro, H. Tributsch, *J. Phys. Chem. B* 101 (1997) 7428–7434.
- [28] B. Enright, D. Fitzmaurice, *J. Phys. Chem. B* 100 (1996) 1027–1035.
- [29] M.R. Hoffmann, S.T. Martin, W. Choi, D.W. Bahnemann, *Chem. Rev.* 95 (1995) 69–96.
- [30] X. Zhang, L. Lei, *Appl. Surf. Sci.* 254 (2008) 2406–2412.
- [31] I.K. Konstantinou, V.A. Sakkas, T.A. Albanis, *Water Res.* 36 (2002) 2733–2742.